Journal Pre-proof

Photoluminescence emissions of $Ca_{1-x}WO_4:xEu^{3+}$: Bridging between experiment and DFT calculations*

Amanda Fernandes Gouveia, Marcelo Assis, Lara Kelly Ribeiro, Aline Estefany Brandão Lima, Eduardo de Oliveira Gomes, Daniele Souza, Yara Gobato Galvão, Ieda Lucia Viana Rosa, Geraldo Eduardo da Luz, Jr., Eva Guillamón, Elson Longo, Juan Andrés, Miguel Angel San-Miguel

PII: S1002-0721(21)00240-4

DOI: https://doi.org/10.1016/j.jre.2021.08.023

Reference: JRE 1095

To appear in: *Journal of Rare Earths*

Received Date: 28 May 2021

Revised Date: 9 August 2021

Accepted Date: 30 August 2021

Please cite this article as: Gouveia AF, Assis M, Ribeiro LK, Brandão Lima AE, de Oliveira Gomes E, Souza D, Galvão YG, Viana Rosa IL, da Luz GE Jr, Guillamón E, Longo E, Andrés J, San-Miguel MA, Photoluminescence emissions of $Ca_{1-x}WO_4:xEu^{3+}$: Bridging between experiment and DFT calculations*, *Journal of Rare Earths*, https://doi.org/10.1016/j.jre.2021.08.023.

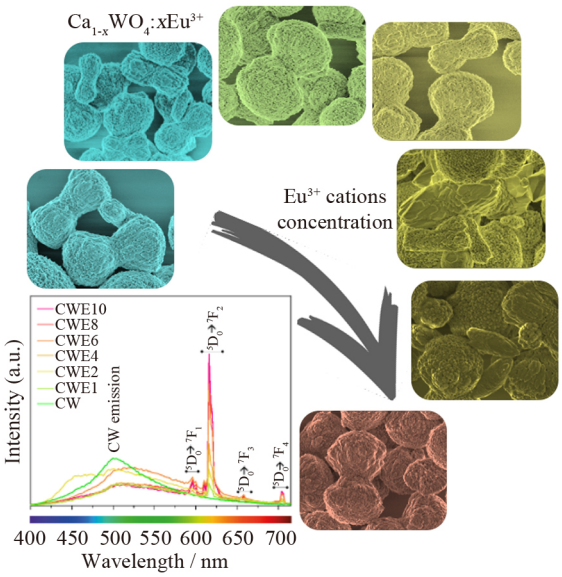

Photoluminescence emissions of $Ca_{1-x}WO_4:xEu^{3+}$: Bridging between experiment and DFT calculations*

Amanda Fernandes Gouveia[a,b,*], Marcelo Assis[a,c], Lara Kelly Ribeiro[c], Aline Estefany Brandão Lima[d], Eduardo de Oliveira Gomes[b], Daniele Souza[e], Yara Gobato Galvão[e], Ieda Lucia Viana Rosa[c], Geraldo Eduardo da Luz Jr[d], Eva Guillamón[a], Elson Longo[c], Juan Andrés[a,*], Miguel Angel San-Miguel[b]

[a]Department of Physical and Analytical Chemistry, University Jaume I (UJI), 12071Castelló, Spain.
[b]Institute of Chemistry, State University of Campinas (Unicamp), 13083-970 Campinas, SP, Brazil.
[c]CDMF, Federal University of São Carlos (UFSCar), P.O. Box 676, 13565-905, São Carlos, São Paulo, Brazil.
[d]Departamento de Química, State University of Piauí (UFPI), 64049-550 Teresina, Piauí, Brazil.
[e]Physics Department, Federal University of São Carlos (UFSCar), P.O. Box 676, 13565-905, São Carlos, São Paulo, Brazil.

ABSTRACT

In this work, the impact of the doping process on the photoluminescence emission of $CaWO_4$ as a function of the concentration of Eu^{3+} cation (0.01 mol%, 0.02 mol%, 0.04 mol%, 0.06 mol%, 0.08 mol%, and 0.10 mol%) is discussed in detail. $Ca_{1-x}WO_4:xEu^{3+}$ samples were successfully synthesized by a simple co-precipitation method followed by microwave irradiation. The blue shift in the absorption edge confirmed the quantum confinement effect and the band gap energy cover the range from 3.91 to 4.18 eV, as the amount of Eu^{3+} cations increases. The experimental results are sustained by first-principles calculations, at the density functional theory level, to decipher the geometry and electronic properties, thereby enabling a more accurate and direct comparison between theory and experiment for the $Ca_{1-x}WO_4:xEu^{3+}$ structure.

* Corresponding author. gouveiad@uji.es

Foundation item: Project supported in part by Fundação de Amparo à Pesquisa do Estado de São Paulo - FAPESP (2013/07296-2; 2016/23891-6; 2017/26105-4; 2019/01732-1), Financiadora de Estudos e Projetos - FINEP, Conselho Nacional de Desenvolvimento Científico e Tecnológico – CNPQ (166281/2017-4, 305792/2020-2), and CAPES.

Keywords: $Ca_{1-x}WO_4:xEu^{3+}$; DFT calculations; photoluminescence emissions; rare earths.

1. Introduction

The high chemical stability of $CaWO_4$ (CW)-based phosphors and the excellent photoluminescence (PL) emissions have attracted a lot of attention due to the ability to serve as a luminescence host with low phonon threshold energy and wide visible emission spectra [1-6].

Lanthanide luminescence has become essential in the lighting industry [7], and the Eu^{3+} cations are the most studied activators in the rare-earth cations (RE^{3+}) family with intense emissions located in the visible region, displaying higher luminescence purity and quantum yields [8-13]. The substitution of Ca^{2+} by Eu^{3+} cations leads to the formation of [EuO_8] clusters. $Ca_{1-x}WO_4$:xEu^{3+} (CWE) doped materials have been obtained through different synthesis methods. Zhang et al. analyzed the effect of synthesis conditions, such as pH, temperature, and doping concentrations, in the morphology and sizes of CWE [14]. Xiong et al. prepared CWE nanoparticles with excellent load-carrying capacity, and friction-reducing properties in a water-soluble [15]. Very recently, the precipitation route to obtain CW nanoparticles containing Eu^{3+} and Dy^{3+} cations were used by Kaur et al. [16].

The changes induced by the addition of Eu^{3+} cations in different concentrations in the CW host matrix increase their performance, due that this material has numerous scientific and technological applications, such as light-emitting diodes converted into phosphors, sensors, capacitors, catalysts and others [15,17-19]. In particular, the CWE samples were previously obtained with different concentration of Eu^{3+} cation and the PL properties as well as the chromaticity coordinates and lifetimes of the samples were investigated [20].

This paper reports a combined experimental and theoretical work to investigate the events that occur in the PL activity and their relationship with the excited electronic states of Eu-doped CW crystals. The main novelty of this study is the use of first-principles quantum-mechanical calculations, at the density functional theory (DFT) level, to study and predict the structure and PL emissions, which would promote the development of CWE based phosphors. The samples were prepared by a simple co-precipitation (CP) method followed by microwave irradiation (MI) without any surfactant. This enabled to be promising materials in inorganic single-emitting component regions for optical applications.

2. Experimental and theoretical procedure

2.1. Synthesis and Characterizations

The synthesis of CW sample was performed using the CP method followed by MI. 1×10^{-3} mol of $Ca(CH_3CO_2)_2\cdot H_2O$ (Aldrich, 99%) and 1×10^{-3} mol of $Na_2WO_4\cdot 2H_2O$ (Aldrich, 99%) were added in two separate beakers containing 50.0 mL of distilled water each. The $Ca(CH_3CO_2)_2\cdot H_2O$ solution was then added to the $Na_2WO_4\cdot 2H_2O$ solution, and the suspension were transferred to a Teflon autoclave, sealed, and placed in the microwave

assisted hydrothermal system (2.45 GHz, maximum power of 800 W). The reaction mixture was heated to 160 °C for 32 min. The products were washed with deionized water several times and dried at 60 °C for 12 h.

For the CWE samples, the same procedure describe above was done with the addition of 0.01 mol%, 0.02 mol%, 0.04 mol%, 0.06 mol%, 0.08 mol%, and 0.10 mol% of Eu^{3+} and the removed of the corresponding Ca^{2+} mass. The reagent used was Eu_2O_3 (Aldrich, 99.9%) dissolved in water from the addition of HNO_3. The doped samples were called by: CWE1, CWE2, CWE4, CWE6, CWE8, and CWE10 for 0.01 mol%, 0.02 mol%, 0.04 mol%, 0.06 mol%, 0.08 mol%, and 0.10 mol% Eu^{3+}, respectively.

The CW and CWE samples were structurally characterized by different techniques such as: X-ray diffraction (XRD) with Rietveld refinement analysis, field emission scanning microscopy (FE-SEM), and spectroscopies of micro-Raman (MR) and Fourier Transform Infrared (FT-IR), ultraviolet-visible (UV-Vis) absorption, energy dispersive (EDS), X-ray photoelectron (XPS), and X-ray fluorescence (XRF).

The XRD using a D/Max-2500PC diffractometer (Rigaku, Japan) with CuK α radiation (λ = 0.15406 nm) in the 2θ range of 10°–110° with a scanning speed of 1 (°)/min. FE-SEM and EDS were performed using an equipment Inspect F50 (FEI Company, Hillsboro, OR), operated at 15 kV. UV-vis diffuse reflectance measurements were obtained using a Cary 5G spectrophotometer (Varian, USA) in diffuse reflection mode. The MR spectra were obtained by the Micro Raman spectrometer (HORIABA Jobin Yvon T64000) with a radiation of 514 nm in the 50–3500 cm^{-1} range. The FT-IR was performed using a Jasco FT/IR-6200 (Japan) spectrophotometer operated in turn mode at room temperature and the spectra were carried out in the range of 470–4000 cm^{-1}. A Kimmon He-Cd laser (325 nm laser; 40 mW maximum power) was used as the excitation source for PL measurements. XPS analyses were performed on a Scientia Omicron ESCA spectrometer (Germany) using a monochromatic X-ray source of Al Kα (1486.7 eV). Peak deconvolution was performed using a 70%:30% Gaussian-Lorentzian line shape and a Shirley nonlinear sigmoid-type baseline. The binding energies of all elements were calibrated with reference to the C 1s peak at 284.8 eV. Element analysis of the samples was performed an XRF 720 (Shimadzu Corp, Kyoto, Japan) operating at 4 kV and 80 mA. The luminescence lifetime measurements were carried out as well using a 1940D model spectrophotometer coupled to the spectrofluorometer.

2.2. Computational Methods

First-principles calculations were performed to study the effect of Eu-doped in the $CaWO_4$ structure. In this way, two models were constructed, the pure CW and CWE. All calculations were performed with the CRYSTAL17 software package [21, 22]. The CRYSTAL package performs *ab initio* calculations of the ground state energy, energy gradient, electronic wave function and properties of periodic systems. Hartree-Fock or KohnSham Hamiltonians (that adopt an Exchange-Correlation potential following the postulates of Density-Functional Theory) can be used. Systems periodic in 0 (molecules, 0D), 1 (polymers, 1D), 2 (slabs, 2D), and 3 dimensions (crystals, 3D) are treated on an equal footing. In each

case the fundamental approximation made is the expansion of the single particle wave functions ('Crystalline Orbital', CO) as a linear combination of Bloch functions (BF) defined in terms of local functions (hereafter indicated as 'Atomic Orbitals', AOs).

The computational method is based on the DFT associated with B3LYP hybrid functional [23,24]. Ca, W, O, and Eu atomic centers were described by the Ag_HAYWSC-311d31G_apra_1991, W_cora_1996, and O_6-31d1_corno_2006 basis sets, respectively, which were obtained from the Crystal website [25,26]. The diagonalization of the Fock matrix was performed using a 6×6×6 grid with 44*k*-point grids in the reciprocal space. The thresholds controlling the accuracy of the calculation of the Coulomb and exchange integrals were set to 10^{-8}, 10^{-8}, 10^{-8}, 10^{-8}, and 10^{-16}, and the percentage of Fock/Kohn–Sham matrix mixing was set to 30.

A full optimization process of the lattice parameters (*a* and *c*) and the internal atomic coordinates (*x*, *y*, and *z*) for the bulk was carried out until all force components were less than 10^{-5} eV/nm^2. From this optimized bulk structure, two periodic models, were built by selecting a 2×2×2 supercell: (1) the pure CW model of 192 atoms in the structure, composed by 32 Ca atoms, 32 W atoms and 128 O atoms and (2) the CWE model, in which two Ca^{2+} cations were replaced by two Eu^{3+} cations. To keep the electroneutrality of the system, a Ca^{2+} cation ghost was considered. This model contains 6.90% molar Eu in the structure. The band structure and density of states (DOS) of de CW and CWE models were obtained for 200 $\vec{k}$ points along the appropriate high-symmetry directions of the corresponding irreducible Brillouin zone.

3. Results and discussion

An analysis of the XRD patterns of the CW and CWE samples in **Fig. 1** renders that all materials exhibit well defined diffraction peaks, corresponding to the scheelite phase with tetragonal structure and space group $I4_1a$; this was in accordance with card No. 5510 [27] in the Inorganic Crystal Structure Database (ICSD). There was no secondary phase formation, indicating that the Eu^{3+} cation substitution process takes places successfully.

Figure 1. XRD patterns of the CW and CWE samples.

From the structural point of view, the lattice of the CW is composed by distorted octahedra [CaO_8] and tetrahedra [WO_4] clusters, in which the Ca atoms are coordinated with eight O atoms in an octahedral symmetry, while the W atoms are surrounded by four O atoms (see **Fig. 2**); each [CaO_8] cluster shares corners with eight [WO_4] tetrahedron to form chains parallel to [110] direction.

Figure 2. CW structure and the distorted octahedra [CaO_8] and tetrahedra [WO_4] clusters. The substitution of the Ca^{2+} by Eu^{3+} cation leads to the formation of [EuO_8] clusters.

Assuming that the samples present a spherical morphology, the average crystallite size (D) and the lattice strain (LS) of the as-synthetized samples were calculated and the values are presented in **Table 1**. The D value was obtained through the Scherrer's equation (**Eqs. (1)-(2)**), using the full width half maximum (FWHM) of the most intense peak [112].

$$D = {0.89\lambda}/{(\beta \cos\theta)} \quad (1)$$

$$\beta = \sqrt{\beta_e^2 - \beta_s^2} \quad (2)$$

where D is the average crystallite size, λ the X-ray wavelength (0.15406 nm), θ the Bragg angle, β_e the experimental full width at half maximum (FWHM) of the sample and β_s the FWHM of LaB_6 standard [28]. The LS parameter[29] can be obtained by Eq. (3):

$$\mathrm{LS} = {\beta}/{(4 \tan\theta)} \quad (3)$$

Table 1. FWHM (°) values, crystallite size (D, nm) and lattice strain (LS, $\varepsilon\times10^{-3}$) calculated from XRD data.

An elemental analysis of the CWE samples were performed by XRF spectrometry to obtain effective amount of Eu^{3+} cations along the doping process at the CW lattice and the results are in **Table 2**. The X-ray energy (spectral line Lα) for the Eu element it was observed in 5.849 keV. The amount of Eu^{3+} cations obtained by XRF compared to the nominal concentration of each sample is very close, confirming the substitution of Ca^{2+} by Eu^{3+} cations in the CW lattice.

Table 2. Amount of Eu^{3+} cations obtained by XRF spectrometry and the nominal value.

The distribution of Ca, W, O and Eu atoms in the CWE10 sample was analyzed by EDS mapping and it was observed a homogeneous distribution for all elements in the observed micro-dumbbells morphology, as can be seen in **Fig. SI-1** (see the Supporting Information, SI).

The XPS technique was used as a powerful tool to qualitatively determine the surface composition of the materials. According to the results (see **Fig. SI-2**), the characteristic peaks of Ca, W and O display that the samples are of high purity and the doping process of Eu^{3+} cations take place at the sites occupied by the Ca^{2+} cations. This analysis also demonstrated that the Eu content in the region close to the surface is much lower than that of the bulk. More details can be found in the XPS section in the SI.

Fig. 3(a) shows the MR spectrum in the range of 50–3500 cm^{-1}. Two different regions can be sensed, one related to $CaWO_4$ (**Fig. 3(b)**) and the other related to Eu substitution (**Fig. 3(c)**) since such modes are observed only with substitution. Both parts of the spectrum presented well defined modes, showing a high degree of order of the samples at short-range. **Fig. 3(b)** shows the spectrum of 50–1000 cm^{-1} in which is related to CW and a full discussion of these modes can be found in the SI. In the spectrum of **Fig. 3(c)**, the bands at 2536.3, 2957.1, 3112.0, and 3195.7 cm^{-1} can be sensed. These bands become even more intense as

the amount of Eu^{3+} cations increases and, according Tiseanu et al., these bands correspond to a fingerprint of substitution by Eu^{3+} cations in a tetragonal structure [30]. The analyses of the FT-IR spectra it was also performed, and the discussion can be found in the SI.

Figure 3. (a) Micro Raman spectra of CW and CWE samples; (b) zoom of the region between 50 and 1000 cm^{-1}; (c) Zoom of the region between 2500 and 3500 cm^{-1}.

For the study of the optical behavior of CWE samples, it was performed by calculating the band gap energy (E_{gap}) using the method proposed by Kubelka and Munk (more details in SI). **Fig. SI-4** shows that the band gap structures of the CW and CWE samples are characteristic of well-defined direct transitions, which is of the nature of crystalline semiconductors. The CW sample presented an E_{gap} of 4.12 eV, the CWE samples presented an E_{gap} of 3.91, 4.01, 4.11, 4.09, 4.10, and 4.18 eV, respectively in ascending order of doping Eu^{+3} cations. The decreasing in the E_{gap} can be attributed to the existence of structural defects localized in the forbidden band gap region.

By using the results of the DFT calculations an analysis of the energy levels in the valence band (VB) and the conduction band (CB) has been performed (see **Fig. 4(a, b)**). As can be seen, a direct electronic transition at the Γ-point in the Brillouin zone can be sensed. The CWE model has a lower band gap value (3.90 eV) when compared with the CW model (5.71 eV). This decrease of the band gap is due to the structural defect caused by the substitution of Ca^{2+} by Eu^{3+} cations, which involves the creation of new energy levels between the VB and CB.

Figure 4. Band structure for (a) CW and (b) CWE models and DOS for **(c)** CW and **(d)** CWE models.

In **Fig. 4(c, d)**, the DOS for the CW and CWE models are displayed, respectively. An analysis of the results renders that despite of the small contribution to CB from the Eu orbitals, the presence of Eu^{3+} cations in the CW structure caused a perturbation in the electronic states into the two bands (VB and CB). The position of Fermi level changed, from −4.40 eV in the CW model to −3.36 eV in the CWE model, while the first empty level in CB, goes from 1.31 to 0.44 eV. In both theoretical models, VB is formed mainly by the 2p orbitals of the O atoms, while CB is composed mainly by the hybridization of the 5d and 2p orbitals, between W and O atoms, respectively.

In order to analyze the morphology of the samples in function of the Eu^{3+} cations concentration, the FE-SEM was performed and images of CW and CWE samples is shown in **Fig. 5**. For the CW sample, the formation of microspheres and micro-dumbbells is observed, with an average size of 4.05 ± 0.49 μm (**Fig. 5(a)**). The microspheres have already been obtained by conventional hydrothermal [31, 32], sonochemical [33] and reverse micelle methods [34]; while the micro-dumbbells morphology was obtained by the microwave hydrothermal method [35]. For the CWE samples (**Fig. 5(b-g)**), the formation of microspheres was not observed, obtaining only micro-dumbbells with sizes of 4.22 ± 0.45, 4.27 ± 0.57,

4.24 ± 0.42, 4.29 ± 0.43, 4.91 ± 0.88, 4.95 ± 0.57 μm for samples CWE1, CWE2, CWE4, CWE6, CWE8, and CWE10, respectively.

Figure 5. FE-SEM images for the samples. (a) CW; (b) CWE1; (c) CWE2; (d) CWE4; (e) CWE6; (f) CWE8; (g) CWE10.

The PL emissions of the samples with different amount of Eu^{3+} cations are displayed in **Fig. 6(a)**. The pure CW has a broadband emission profile, characteristic of a multiphonic process, involving several intermediate energy states. The maximum emission of the CW sample is found in approximately 500 nm, in the cyan-green region, which are the result of internal charge transfers from the $[WO_4]$ clusters and oxygen vacancy (V_O) in the $[WO_4]$ and $[CaO_8]$ clusters [4, 36]. With the replacement of Ca^{2+} by Eu^{3+} cations, the appearance of specific transitions of Eu^{3+} is observed ($^5D_0 \rightarrow {}^7F_j$, j = 1, 2, 3, and 4), with maximum emission located at 596, 616, 659, and 704 nm, and these become more intense with the increased concentration of Eu^{3+} cations (**Fig. 6(a)**) [37]. The intensities of the observed transitions are dependent on the coordination of the Eu^{3+} cations [38].

Figure 6. (a) PL spectra for CW and CWE samples (λ = 350 nm); (b) Ratio of relative area for transitions $^5D_0 \rightarrow {}^7F_2$ / $^5D_0 \rightarrow {}^7F_1$; (c) Schematic luminescence model of CWE samples; (d) Coordinates of the Commission Internationale de l'Eclairage (CIE) by Spectralux software.

The peak located at 596 nm comes from a magnetic dipole transition $^5D_0 \rightarrow {}^7F_1$, that were almost independent of the local environment. The peak of greatest intensity, located at 616 nm, is called a hypersensitive red emission, and it comes from the transition of electric dipole $^5D_0 \rightarrow {}^7F_2$, that was strongly dependent of the environment. The appearance of this transition suggests that the Eu^{3+} cation is located in a symmetrical site where there is no inversion of symmetry [39], while the absence of the transition $^5D_0 \rightarrow {}^7F_0$ implies that the Eu^{3+} cations are not occupying sites with C_s, C_n or C_{nv} symmetry [40]. The ratio of relative area of the $^5D_0 \rightarrow {}^7F_2$ to $^5D_0 \rightarrow {}^7F_1$ transitions provides information about the local distortions in the clusters which the Eu^{3+} cations were inserted into the structure [41]. As presented in **Fig. 6(b)**, when increasing the concentration of Eu^{3+} in the CWE samples, there is an increase in local distortions related to the $[EuO_8]$ clusters of the crystalline lattice.

Fig. 6(c) shows the schematic luminescence model of CWE samples. When the sample is excited, electrons are promoted from the VB, made up of the O 2p levels, to the CW CB, made up of the W 5d levels. The emission of these samples occurs when the excited electrons decay radiative from the CB to the VB, or when the transfer of electrons from the CB to the excited levels of the Eu^{3+} cations. When populated, 4f states decay non-radiative to the level of emission characteristic of the Eu^{3+} cations ($^5D_0$) and then radiative to the fundamental states (^7F_j, j = 1, 2, 3, and 4), emitting in the observed characteristic lengths.

The change in the color emission perceptible by the human eye of the CW and CWE samples were evaluated by the coordinates of the Commission Internationale de l'Eclairage

(CIE) by Spectralux software [42] from the emission spectra obtained at under laser excitation at 350 nm (**Fig. 6(d)**). As expected, the CW has an emission in the cyan-green region, with a shift to orange with an increase in the substitution of Ca^{2+} by Eu^{3+} cations. This change occurs due to the sum of the characteristic emissions of Eu^{3+} cations in the red region ($^5D_0 \rightarrow {}^7F_j$, j = 1, 2, 3, and 4) with the emissions of the CW matrix. Therefore, the ions substitution in a semiconductor matrix by Eu^{3+} cations can lead to modulation of the final characteristic emission, resulting in potential materials for application in optical devices.

The lifetimes of the CWE samples were calculated for the luminescence decay of $^5D_0 \rightarrow {}^7F_2$ transition, with emission and excitation fixed at 616 and 394 nm, respectively. **Fig. SI-5** shows the mono exponential decay of the samples fitted with an exponential function as the **Eq. (4)**:

$$y = y_0 + A_1 \exp(t/\tau) \quad (4)$$

Where, y is the intensity, y_0 the intensity at the 0 ms, A_1 the amplitude, and τ the lifetime of the transition $^5D_0 \rightarrow {}^7F_2$.

The τ values obtained for the CWE samples were close, being 0.70 ± 0.04, 0.70 ± 0.04, 0.72 ± 0.03, 0.72 ± 0.02, 0.70 ± 0.01, and 0.67 ± 0.01 ms for samples CWE1, CWE2, CWE4, CWE6, CWE8, and CWE10, respectively. The CWE samples were fitted to a linear fit of lg$y$ versus t, indicating the samples have only one time of decay (see **Fig. SI-5**). These results indicate that Eu^{3+} cations occupy only one place of symmetry in the CW matrix and that there is only one process for the luminescence of the CWE samples.

4. Conclusions

In summary, the present work combines the experimental and theoretical results for better understanding of the PL emissions of the CW and CWE samples with different Eu^{3+} cations concentration. First-principles calculations, within the framework of DFT, were performed to achieve a deeper understanding of the effects caused by the Eu^{3+} cations in the CW electronic structure in order to correlate with the PL emissions experimentally observed. These findings allow to find a luminescent material in which by varying the Eu^{3+} cations concentration, the color emissions can be modulated. This work also paves the way for the further design of CWE-based materials for various applications as red-blue phosphors in different kinds of display devices.

Declaration of competing interest

The authors declare that they have no known competing financial interests or personal relationships that could have appeared to influence the work reported in this paper.

Acknowledgements

This work was funded in part by Fundação de Amparo à Pesquisa do Estado de São Paulo - FAPESP (2013/07296-2; 2016/23891-6; 2017/26105-4; 2019/01732-1), Financiadora de Estudos e Projetos - FINEP, Conselho Nacional de Desenvolvimento Científico e Tecnológico – CNPQ (166281/2017-4, 305792/2020-2), and CAPES. This work used computational resources of the "Centro Nacional de Processamento de Alto Desempenho em São Paulo" (CENAPAD-SP), "Centro de Computação John David Rogers" (CCJDR-UNICAMP), and the CENAPAD-RJ (SDumont). J.A. acknowledges Universitat Jaume I (project UJI-B2019-30), and the Ministerio de Ciencia, Innovación y Universidades (Spain) (project PGC2018094417-B-I00) for financially supporting this research.

Appendix A. Supplementary data

Supplementary data to this article can be found online.

References

1. Yu MQ, Xu HY, Li YZ, Dai QL, Wang GF, Qin WP. Morphology luminescence and photovoltaic performance of lanthanide doped $CaWO_4$ nanocrystals. J Colloid Interface Sci. 2020; 559:162.
2. Chai RT, Liu YT, Zhang G, Feng JJ, Kang QW. In situ preparation and luminescence properties of $CaWO_4$ and $CaWO_4$:Ln (Ln=Eu^{3+}, Tb^{3+}) nanoparticles and transparent $CaWO_4$:Ln/PMMA nanocomposites. J Lumin. 2018; 202:65.
3. Bae Y-J, Lee KH, Byeon S-H. Synthesis and Eu^{3+} concentration-dependent photoluminescence of $Gd_{2-x}Eu_xO_3$ nanowires. J Lumin. 2009; 129:81.
4. Gracia L, Longo VM, Cavalcante LS, Beltran A, Avansi W, Li MS, et al. Presence of excited electronic state in $CaWO_4$ crystals provoked by a tetrahedral distortion: An experimental and theoretical investigation. J Appl Phys. 2011; 110:043501.
5. Longo VM, Cavalcante LS, Paris EC, Sczancoski JC, Pizani PS, Li MS, et al. Hierarchical Assembly of $CaMoO_4$ Nano-Octahedrons and Their Photoluminescence Properties. J Phys Chem C. 2011; 115:5207.
6. Luo XF, Xie RJ. Recent progress on discovery of novel phosphors for solid state lighting. J. Rare Earths. 2020; 38:464.
7. Bunzli JCG, Wang XJ, Chen XY. Preface to the Special Issue of Rare Earth Luminescent Materials. J Rare Earths. 2020; 38:I.
8. Bunzli JCG. On the design of highly luminescent lanthanide complexes. Coord Chem Rev. 2015; 293:19.
9. Zhu HM, Lin CC, Luo WQ, Shu ST, Liu ZG, Liu YS, et al. Highly efficient non-rare-earth red emitting phosphor for warm white light-emitting diodes. Nat Commun. 2014; 5:4312.
10. Carlos LD, Ferreira RAS, Bermudez VD, Ribeiro SJL. Lanthanide-Containing Light-Emitting Organic-Inorganic Hybrids: A Bet on the Future. Adv Mater 2009; 21:509.

11. Richards BS. Luminescent layers for enhanced silicon solar cell performance: Down-conversion. Sol Energy Mater Sol Cells. 2006; 90:1189.
12. Kang FW, Li LJ, Han J, Lei DY, Peng MY. Emission color tuning through manipulating the energy transfer from VO_4^{3-} to Eu^{3+} in single-phased $LuVO_4:Eu^{3+}$ phosphors. J Mater Chem C. 2017; 5:390.
13. Xie W, Mo YW, Zou CW, Kang FW, Sun GH. Broad color tuning and Eu^{3+}-related photo-emission enhancement via controllable energy transfer in the $La_2MgGeO_6:Eu^{3+},Bi^{3+}$ phosphor. Inorg Chem Front. 2018; 5:1076.
14. Zhang Y, Abraha A, Zhang R, Shahbazyan T, Fadavi M, Heydari E, et al. Luminescence properties of $CaWO_4$ and $CaWO_4:Eu^{3+}$ nanostructures prepared at low temperature. Opt Mater. 2018; 84:115.
15. Xiong S, Liang D, Wu H, Lin W, Chen JS, Zhang BS. Preparation, characterization, tribological and lubrication performances of Eu doped $CaWO_4$ nanoparticle as anti-wear additive in water-soluble fluid for steel strip during hot rolling. Appl Surf Sci. 2021; 539:148090.
16. Kaur P, Khanna A, Fabian M. Effects of annealing temperature on structural and photoluminescence properties of Eu, Dy and Sm doped $CaWO_4$ nanoparticles. Ceram Int. 2020; 46:27262.
17. Kaur P, Khanna A, Kaur J, Kumar R, Chandra R. Rare earth doped $CaWO_4$ and $CaMoO_4$ thin films for white light emission. J Vac Sci Technol B. 2021; 39:012205.
18. Singh M, Ul Haq W, Bishnoi S, Singh BP, Arya S, Khosla A, et al. Investigating photoluminescence properties of Eu^{3+} doped $CaWO_4$ nanoparticles via Bi^{3+} amalgamation for w-LEDs application. Mater Technol. DOI: 10.1080/10667857.2021.1918866
19. Oliveira MC, Ribeiro RAP, Gracia L, Lazaro SR, Assis M, Oliva M, et al. Experimental and theoretical study of the energetic, morphological, and photoluminescence properties of $CaZrO_3:Eu^{3+}$. Crystengcomm. 2018; 20:5519.
20. Goncalves RF, Cavalcante LS, Nogueira IC, Longo E, Godinho MJ, Sczancoski JC, et al. Rietveld refinement, cluster modelling, growth mechanism and photoluminescence properties of $CaWO_4:Eu^{3+}$ microcrystals. CrystEngComm. 2015; 17:1654.
21. Dovesi R, Erba A, Orlando R, Zicovich-Wilson CM, Civalleri B, Maschio L, et al. Quantum-mechanical condensed matter simulations with CRYSTAL. Wiley Interdisciplinary Reviews-Computational Molecular Science. 2018; 8:1.
22. Dovesi R, Saunders VR, Roetti C, Orlando R, Zicovich-Wilson CM, Pascale F, et al., CRYSTAL17 User's Manual. University of Torino. 2017, Torino.
23. Becke AD. Density-Functional Thermochemistry .3. The Role of Exact Exchange. J Chem Phys. 1993; 98:5648.
24. Lee CT, Yang WT, Parr RG. Development of the Colle-Salvetti Correlation-Energy Formula into a Functional of the Electron-Density. Phys Rev B: Condens Matter Mater Phys. 1988; 37:785.
25. Dovesi R, Orlando R, Civalleri B, Roetti C, Saunders VR, Zicovich-Wilson CM. *Crystal Basis Sets Library*. <http://www.crystal.unito.it/basis-sets.php>.

26. Crystal. Basis Sets Library. http://www.crystal.unito.it/Basis_Sets/Ptable.html.
27. Gomez GE, Lopez CA, Ayscue RL, Knope KE, Deluigi MDT, Narda GE. Strong photoluminescence and sensing performance of nanosized $Ca_{(0.8)}Ln_{(0.1)}Na_{(0.1)}WO_{(4)}$ (Ln = Sm,Eu) compounds obtained by the dry "top-down" grinding method. Dalton Trans. 2019; 48:12080.
28. Klug HP, Alexander LE. X-Ray Diffraction Procedures: For Polycrystalline and Amorphous Materials. 2nd Edition ed. 1974: Wiley-VCH.
29. Jayachandraiah C, Kumar KS, Krishnaiah G, Rao NM. Influence of Dy dopant on structural and photoluminescence of Dy-doped ZnO nanoparticles. J Alloys Compd. 2015; 623:248.
30. Tiseanu C, Cojocaru B, Parvulescu VI, Sanchez-Dominguez M, Primus PA, Boutonnet M. Order and disorder effects in nano-ZrO_2 investigated by micro-Raman and spectrally and temporarily resolved photoluminescence. Phys Chem Chem Phys. 2012; 14:12970.
31. Ningombam GS, Nongmaithem RS. Morphology and photoluminescence of self-assembled $CaWO_4:Sm^{3+}$ microspheres: effect of pH and surfactant concentration. Int Nano Lett. 2017; 7:133.
32. Chen GQ, Wang FL, Ji WC, Liu YX, Zhang X. Improved luminescence of $CaWO_4:Eu^{3+}$ microspheres by codoping Gd^{3+}. Superlattice Microst. 2016; 90:30.
33. Janbua J, Mayamae J, Wirunchit S, Baitahe R, Vittayakorn N. Directed synthesis, growth process and optical properties of monodispersed $CaWO_4$ microspheres via a sonochemical route. RSC Adv. 2015; 5:19893.
34. Ningombam GS, Singh NR, Ningthoujam RS. Controlled synthesis of $CaWO_4:Sm^{3+}$ microsphere particles by a reverse-micelle method and their energy transfer rate in luminescence. Colloids Surfaces A: Physicochem Eng Aspects. 2017; 518:249.
35. Goncalves RF, Godinho MJ, Marques APA, Santos MRC, Rosa ILV, Longo E, et al. Structure, Morphology, and Optical Properties of $(Ca_{(1-3x)}Eu_{(2x)})WO_4$ Microcrystals. Electron Mater Lett. 2015; 11:193.
36. Cavalcante LS, Longo VM, Sczancoski JC, Almeida MAP, Batista AA, Varela JA, et al. Electronic structure, growth mechanism and photoluminescence of $CaWO_4$ crystals. CrystEngComm. 2012; 14:853.
37. Mazzo TM, Pinatti IM, Macario LR, Avansi W, Moreira ML, Rosa ILV, et al. Europium-doped calcium titanate: Optical and structural evaluations. J Alloys Compd. 2014; 585:154.
38. Wang WX, Yang PP, Gai SL, Niu N, He F, Lin J. Fabrication and luminescent properties of $CaWO_4:Ln(^{3+})$ (Ln = Eu, Sm, Dy) nanocrystals. J Nanopart Res. 2010; 12:2295.
39. Pinatti IM, Nogueira IC, Pereira WS, Pereira PFS, Gonçalves RF, Varela JA, et al. Structural and Photoluminescence Properties of Eu^{3+} Doped α-Ag_2WO_4 Synthesized by the Green Coprecipitation Methodology. Dalton Trans. 2015; 44:17673.
40. Su YG, Li LP, Li GS. Synthesis and Optimum Luminescence of $CaWO_4$-Based Red Phosphors with Codoping of Eu^{3+} and Na^+. Chem Mater. 2008; 20:6060.
41. Volanti DP, Rosa ILV, Paris EC, Paskocimas CA, Pizani PS, Varela JA, et al. The role of the Eu^{3+} ions in structure and photoluminescence properties of $SrBi_2Nb_2O_9$ powders. Opt Mater. 2009; 31:995.

42. Stearns EI. *Commission Internationale de L'Éclairage, Colorimetry. Color Res. Appl.* 2nd ed ed. Central Bureau of the CIE. Vol. 13. 1987, Gaithersburg, MD: Publication CIE No. 15.2, 78; Central Bureau of the CIE.

Table of Content

The impact of the doping process on the photoluminescence emission of $CaWO_4$ as a function of the concentration of Eu^{3+} cation is discussed in detail, and first-principles calculations endorsed the experimental results.

Table 1. FWHM (°) values, crystallite size (D, nm) and lattice strain (LS, $\varepsilon.10^{-3}$) calculated from XRD data.

Sample	FWHM (°)	D (nm)	LS ($\varepsilon.10^{-3}$)
CW	0.297	28.819	10.249
CWE1	0.276	31.018	6.030
CWE2	0.293	29.217	7.510
CWE4	0.299	28.626	10.318
CWE6	0.395	21.672	10.124
CWE8	0.294	29.116	8.279
CWE10	0.287	29.829	6.270

Table 2. Amount of Eu^{3+} cations obtained by XRF spectrometry and the nominal value.

Sample	Experimental	Nominal
CW	0.0000	0.0000
CWE1	0.0112	0.0100
CWE2	0.0181	0.0200
CWE4	0.0409	0.0400
CWE6	0.0571	0.0600
CWE8	0.0816	0.0800
CW10	0.0972	0.1000

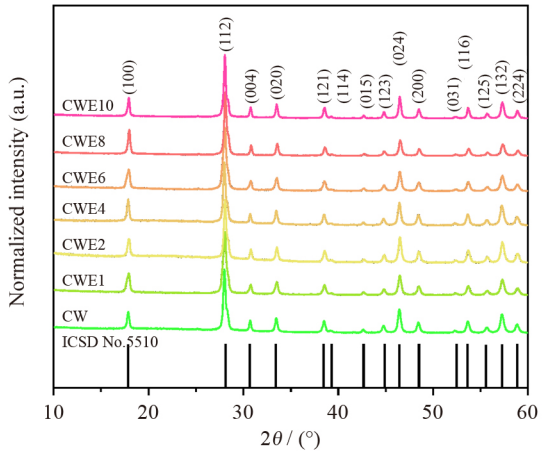

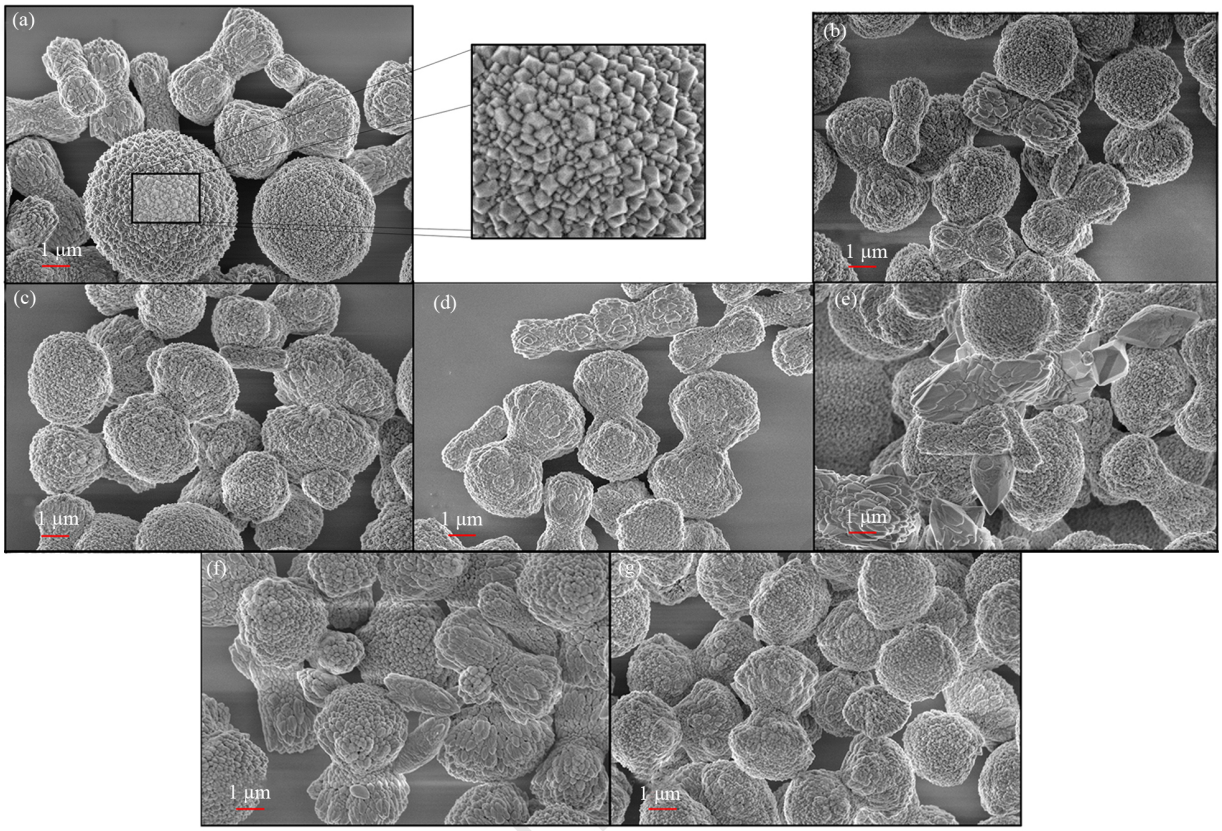

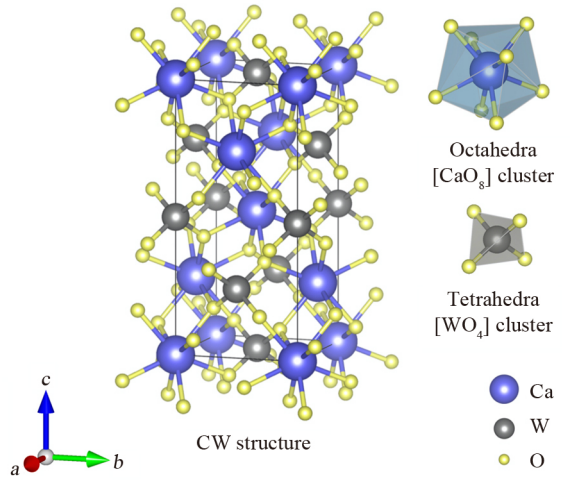

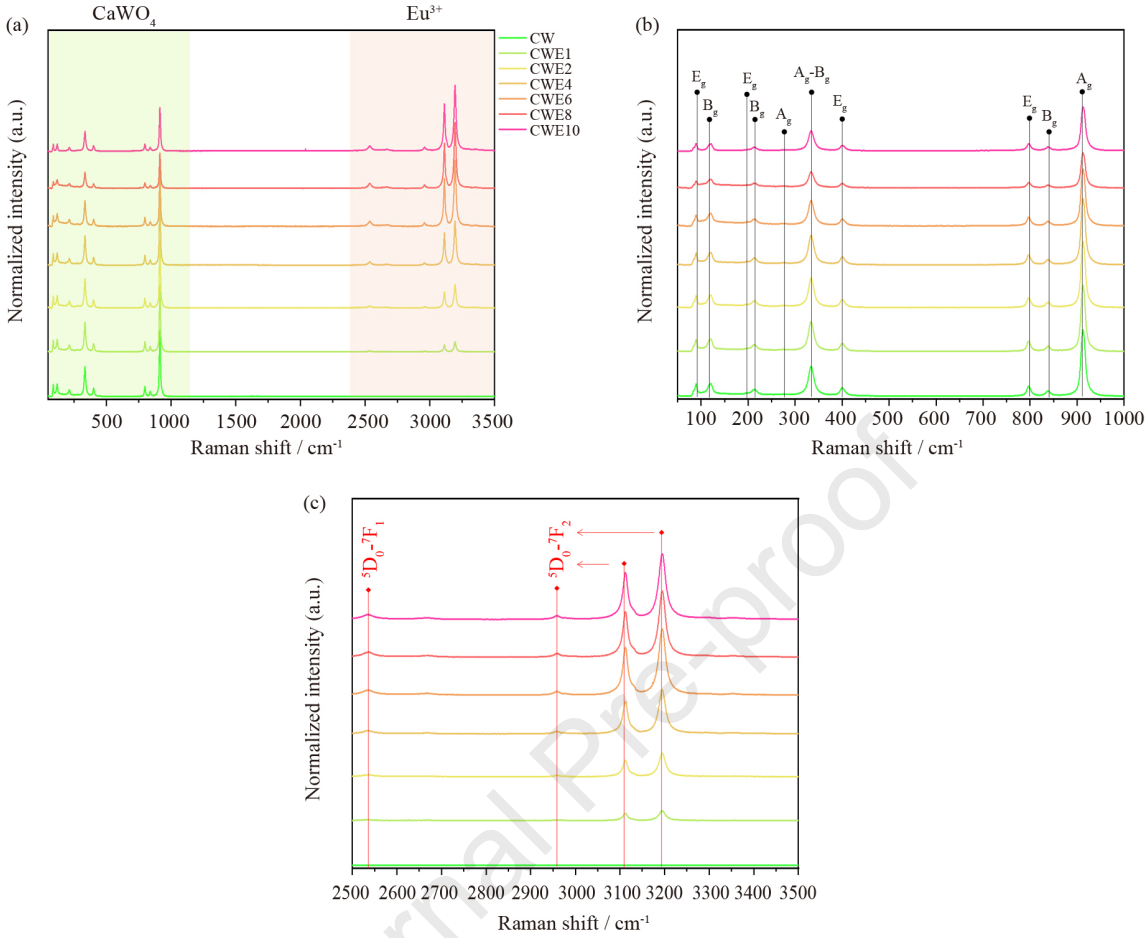

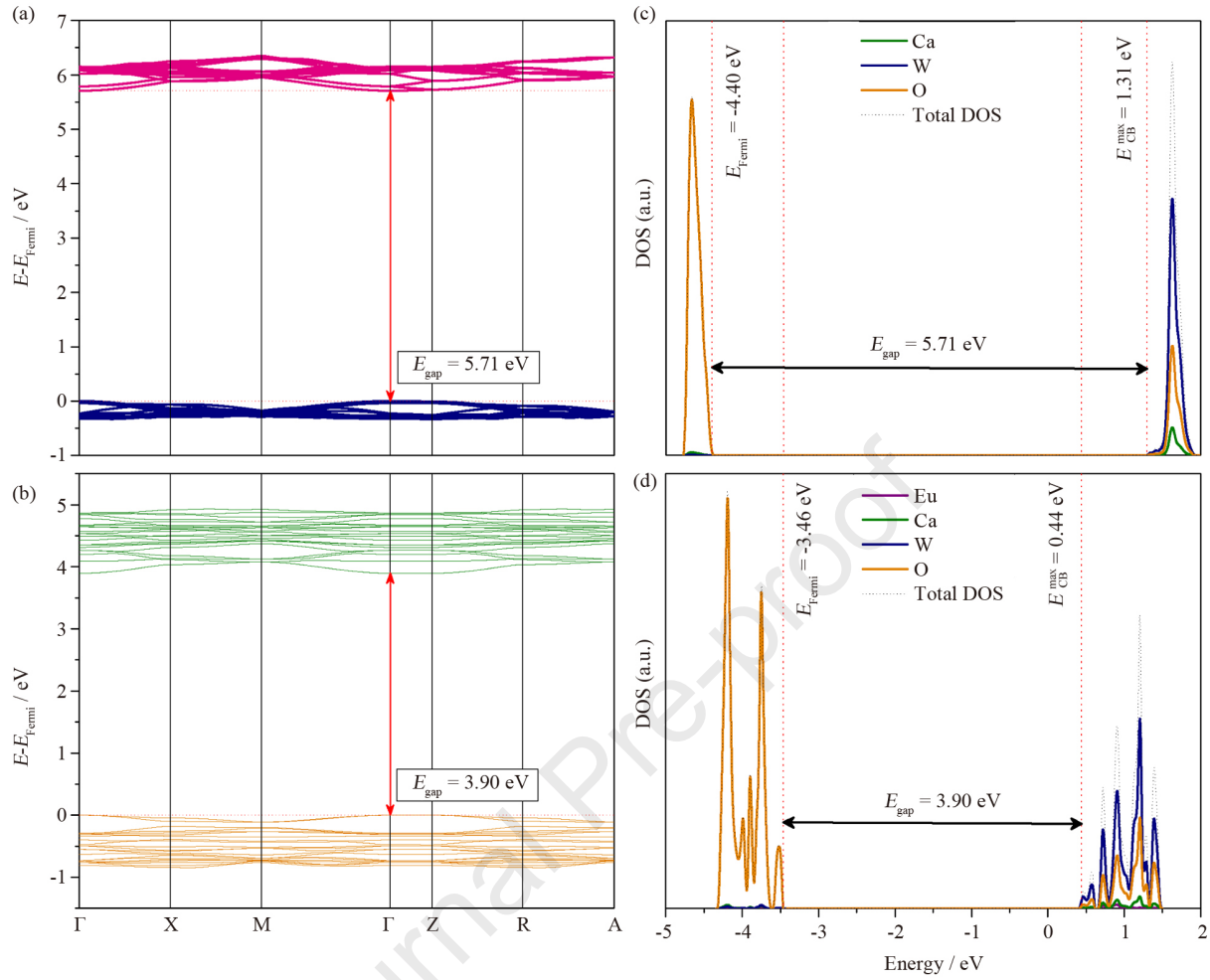

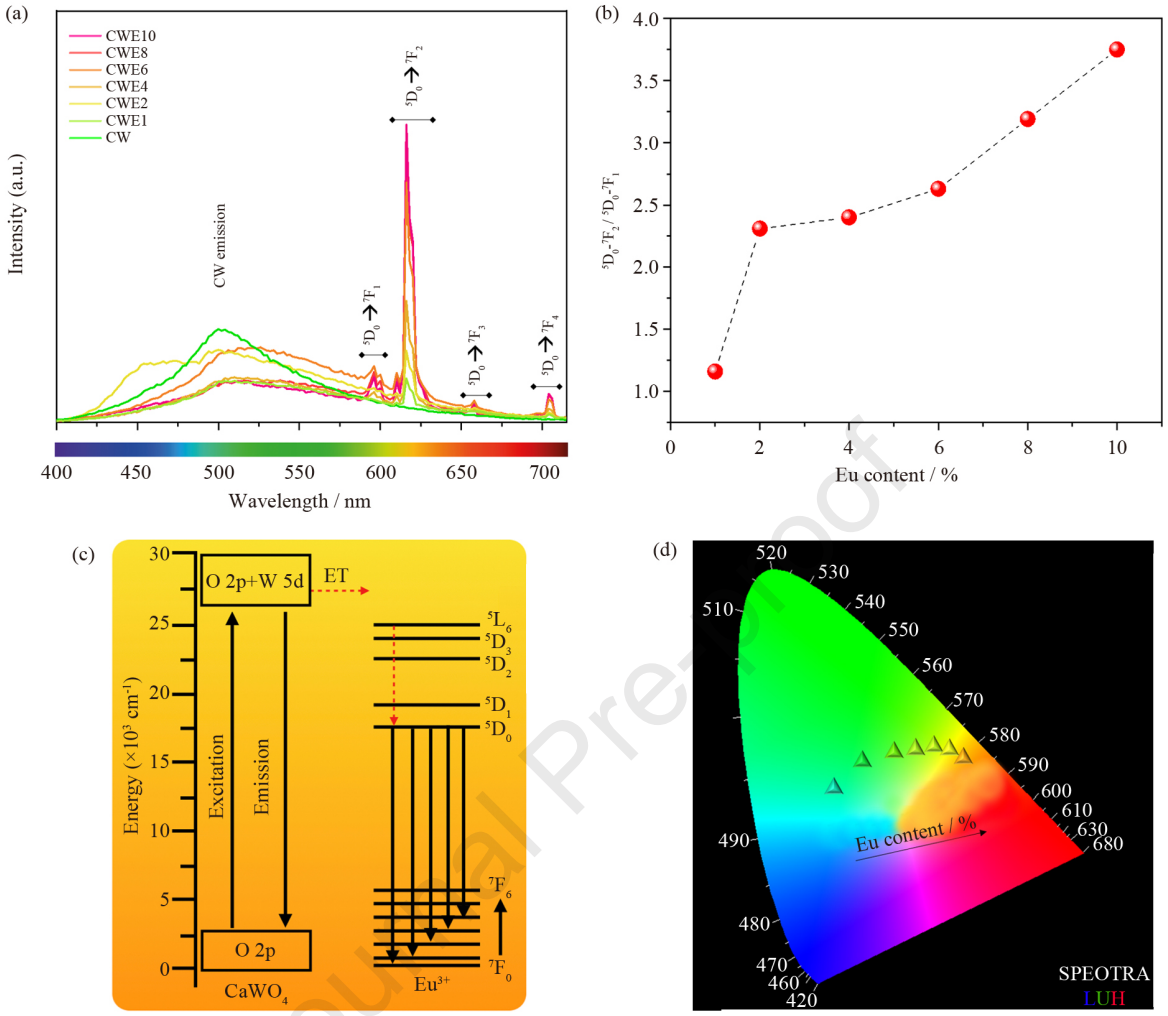

Declaration of interests

☒ The authors declare that they have no known competing financial interests or personal relationships that could have appeared to influence the work reported in this paper.

☐The authors declare the following financial interests/personal relationships which may be considered as potential competing interests:

Photoluminescence emissions of $Ca_{1-x}WO_4:xEu^{3+}$: Bridging between experiment and DFT calculations

Amanda Fernandes Gouveia[a,b,*], Marcelo Assis[a,c], Lara Kelly Ribeiro[c], Aline Estefany Brandão Lima[d], Eduardo de Oliveira Gomes[b], Daniele Souza[e], Yara Gobato Galvão[e], Ieda Lucia Viana Rosa[c], Geraldo Eduardo da Luz Jr[d], Eva Guillamón[a], Elson Longo[c], Juan Andrés[a,*], Miguel Angel San-Miguel[b]

[a]Department of Physical and Analytical Chemistry, University Jaume I (UJI), 12071Castelló, Spain.
[b]Institute of Chemistry, State University of Campinas (Unicamp), 13083-970 Campinas, SP, Brazil.
[c]CDMF, Federal University of São Carlos (UFSCar), P.O. Box 676, 13565-905, São Carlos, São Paulo, Brazil.
[d]Departamento de Química, Federal University of Piauí (UFPI), 64049-550 Teresina, Piauí, Brazil.
[e]Physics Department, Federal University of São Carlos (UFSCar), P.O. Box 676, 13565-905, São Carlos, São Paulo, Brazil.

Supporting Information

EDS mapping

To analyze the distribution of Ca, W, O, and Eu atoms in the CWE samples, an EDS mapping was performed. **Figure SI-1** illustrated the mapping for the CWE10 sample and in this analysis, it was possible to observe a homogeneous distribution for all elements in the observed micro-dumbbells morphology. This distribution indicates a delocalized substitution of Eu^{3+} cations throughout the sample, corroborating with the XRD analyzes, where it is not observed the formation of secondary phases from the replacement of Ca^{2+} by Eu^{3+} cations.

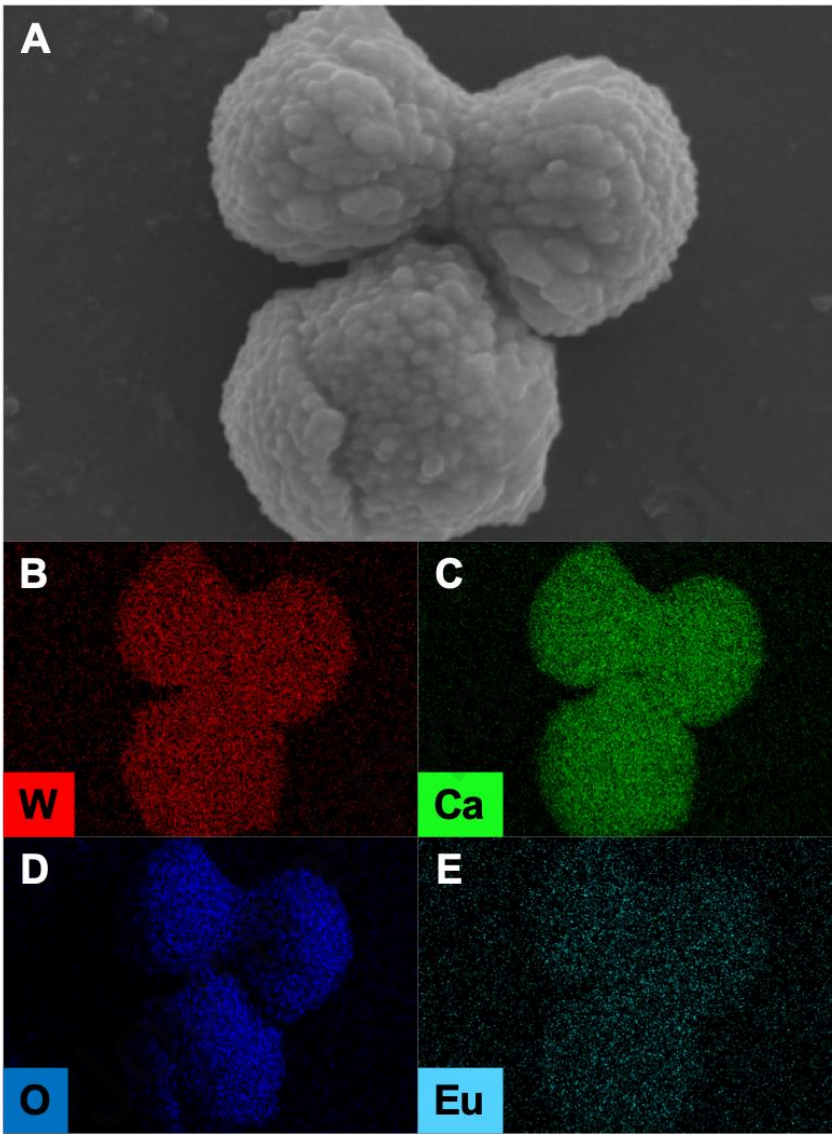

Figure SI-1. EDS mapping for the CWE10 sample.

X-ray photoelectron

In **Figure SI-2A**, the XPS spectrum of the survey of CW and CWE samples show the presence of a large amount of C (derived from the sample holder) and the characteristic peaks of Ca, W and O atoms, indicating that the samples are of high purity. The binding energy (calibrated using C (1*s*, 284.7 eV) as a reference) is shown for the Ca (2*p*, ~346.7 eV), W (4*f*, ~34.8 eV) and O (1*s*, ~530.25 eV) atoms.

The scan of the binding energy survey of the Ca, W and O core of the CW and CWE samples, in the range 0–1200 eV, are shown in **Figure SI-2B-H**. The XPS spectra of Ca (2*p*) were obtained in the range of 339 to 358 eV. In **Figure SI-2B(a)**, for the CW samples, the peak corresponding to Ca (2*p*) has a core binding energy of 346.2 eV ($2p_{3/2}$) and 349.6 eV ($2p_{1/2}$) with full width the half maximum (FWHM) of 1.7 and 2.09 eV, respectively. These results confirm the +2 oxidation state of Ca present in the structure [1, 2]. For CWE samples, in **Figure SI-2C(a)-H(a)**, the peaks corresponding to Ca (2*p*) have a core binding energy that varies from 346 to 348 eV for the $2p_{3/2}$ state and from 349 to 351 eV for the state of $2p_{1/2}$. These shifts in the binding energies of the Ca nucleus for the CWE samples indicate that the presence of Eu generates changes in the effective charge felt by the internal electrons, thus occurring an increase in the binding energies [3, 4].

The XPS spectra of W atoms (4*f*) were observed in the range 30–46 eV. In **Figure SI-2B(b)**, for the CW samples, the peak corresponding to W (4*f*) has a core binding energy of 34.4 eV ($4f_{7/2}$) and 36.4 eV ($4f_{5/2}$) with FWHM of 1.9 and 1.4 eV, respectively. For CWE samples, in **Figure SI-2C(b)-H(b)**, the peaks corresponding to W (4*f*) have a core binding energy that varies from 34 to 35 eV for the $4f_{7/2}$ state and from 36 to 37 eV for the state of $4f_{5/2}$. These results indicate that the oxidation state of W in the structure corresponds to +6 [4].

The XPS spectra of O atoms (1*s*) were observed in the range 525–535 eV. In **Figure SI-2B(c)**, for the CW samples, the peak corresponding to O (1*s*), these materials calcium-based oxygen carriers by possess were three types of oxygen species: surface adsorbed oxygen (O_{ads}), surface lattice oxygen ($O_{surf\text{-}lat}$), and bulk lattice oxygen ($O_{lattice\text{-}bulk}$) [5-8]. In **Figure SI-2C(c)-H(c)** it is possible to verify that these three species were also identified in the CWE samples, being able to attribute the peak of the photoelectron with binding energy located at approximately 529 eV to oxygen in the network ($O_{lattice\text{-}bulk}$), the second peak of the

photoelectron with binding energy located around 530-531 eV surface oxygen of the network ($O_{surf\text{-}lat}$), while the third photoelectron in 531-533 eV was attributed to the oxygen adsorbed on the surface (O_{ads}). In the CWE samples, the peak intensity of (O_{ads}) increased with the increase of Eu^{3+} doping. This increase in peak intensity (O_{ads}) may be due to the fact that oxygen vacancies caused by the insertion of Eu^{3+} cations can capture more species in the environment, such as carbonates and hydroxides [7, 9]. Although it is not possible to observe the presence of Eu 3*d*/4*d* in the survey spectrum, a high-resolution spectrum was applied in the region of 120-180 eV (Eu 4*d*) [10]. In the XPS technique the penetration layer is ~ 3 nm and if the sample has low concentration and few atoms in the surface in relation to the bulk, the signal will be of low intensity.

It can be observed in **Figure SI-2C(d)-H(d)** that the peak signal of the photoelectron with binding energy located around 120-180 eV referring to Eu 4*d* appears with the increase in doping performed on the $CaWO_4$ structure. The replacement of Eu atoms at the Ca^{2+} sites take place in the +3 oxidation state. That the doping occurred with the replacement of Eu^{3+} ions in the Ca^{2+} sites and that the Eu content in the region close to the surface is much lower than that of the bulk.

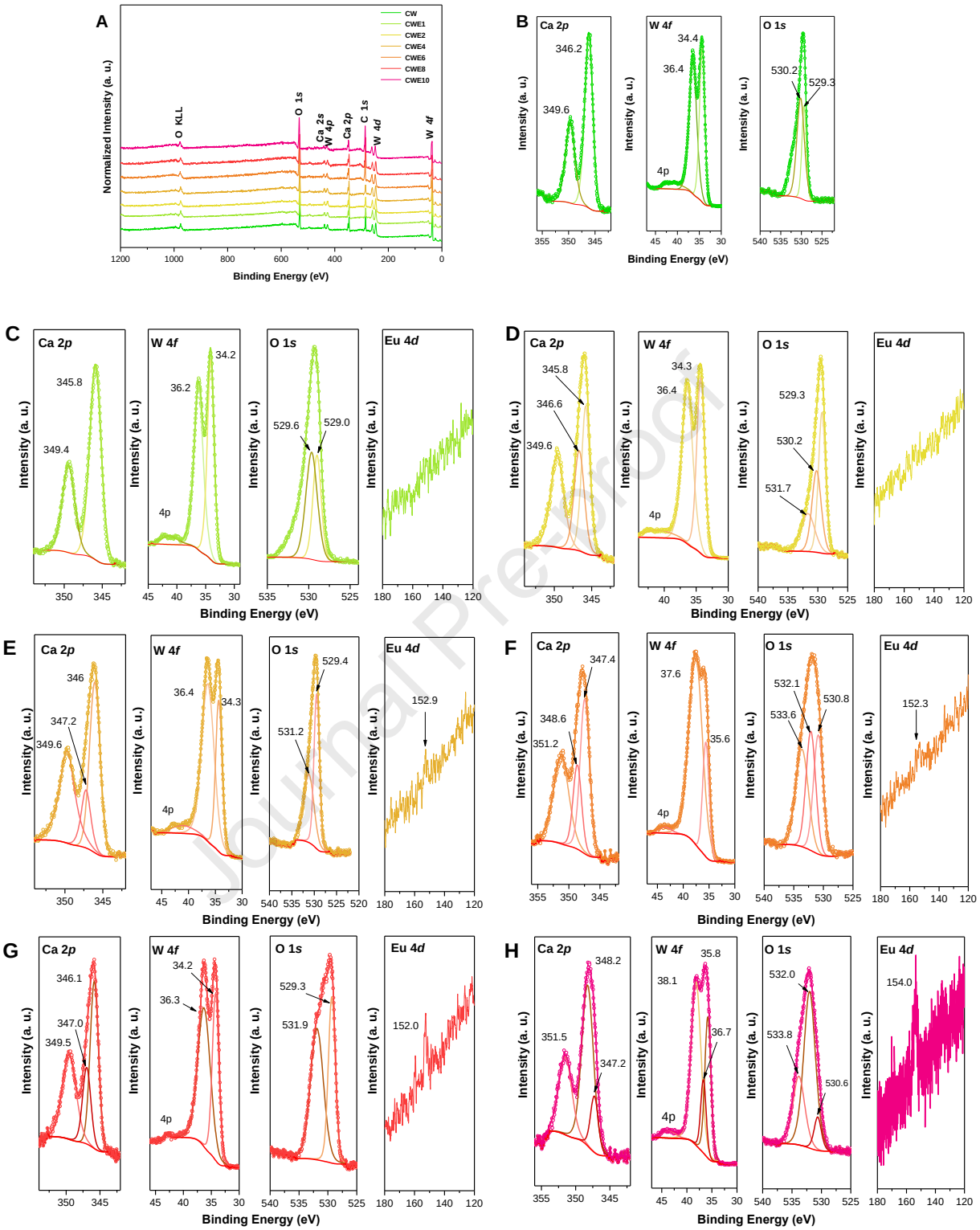

Figure SI-2. A) Survey XPS spectra for CW and CWE samples. **B-H**) High XPS spectra of Ca, W and O for CW samples and Ca, W, O and Eu for CWE samples. The figures are followed by **B)** CW, **C)** CWE1, **D)** CWE2, **E)** CWE4, **F)** CWE6, **G)** CWE8, and **H)** CWE10 samples.

Micro-Raman

According to group theory analysis, the allowed representation for each of the corresponding Wyckoff positions of the tetragonal $CaWO_4$ structure indicates 13 active Raman modes corresponding to the decomposition at the point $\Gamma = (3A_g + 5Bg + 5E_g)$ [11, 12]. A total of 11 active Raman modes are observed, related to $3A_g$ vibrations (275.3, 333.9 and 914.0 cm^{-1}), $4B_g$ vibrations (121.5, 213.1, 333.9, and 838.0 cm^{-1}) and $4E_g$ vibrations (88.6, 193.6, 400.0, and 797.3 cm^{-1}). The bands observed at 88.6 and 213.1 cm^{-1} are related to symmetric bending and stretching of the $[CaO_8]$ clusters [13]. The $[WO_4]$ clusters has T_d symmetry, which can be decomposed into 4 internal modes (ν_1, ν_2, ν_3, ν_4), a rotational mode ($\nu_{f.r}$) and a translational mode [11, 14]. The bands observed in 121.5, 193.6 and 275.3 cm^{-1} are related to translational and free rotation modes of the $[WO_4]$ clusters [15, 16]. The bands located at 333.9 and 400.0 cm^{-1} are related to symmetrical (ν_2) and asymmetrical bending (ν_4) of the O–W–O bond angles [11, 15]. The bands located at 729.3 and 838.00 cm^{-1} are related to asymmetric stretching (ν_3) of the O–W–O bonds [11]. Finally, the most intense band located in 914.0 cm^{-1} is related to the symmetric stretching (ν_3) of the W–O bonds [15].

Fourier Transform Infrared

Figure SI-3 illustrates the FT-IR spectra with the corresponding positions of IR-active modes of CWE samples. The scheelite-type structure has eight stretching and/or bending IR-active vibrational modes [13], presented by $\Gamma = (4A_u + 4E_u)$. Only three modes were identified for the CW and CWE samples in the range from 400 to 3500 cm^{-1}. Firstly, the CW and CWE samples exhibited a 443 cm^{-1} band that are assigned to the υ_4 $A_u + E_u$ mode that arise from symmetric bending vibrations with in the $[WO_4]$ clusters. The modes located at 802 and 849 cm^{-1} are attributed to an overlapping of two intense bands referring to υ_4 A_u and E_u,

respectively, which were ascribed to the O–W–O anti-symmetric stretching vibrations with in the [WO_4] clusters. The band located at 3153 cm^{-1} refer to OH stretching.

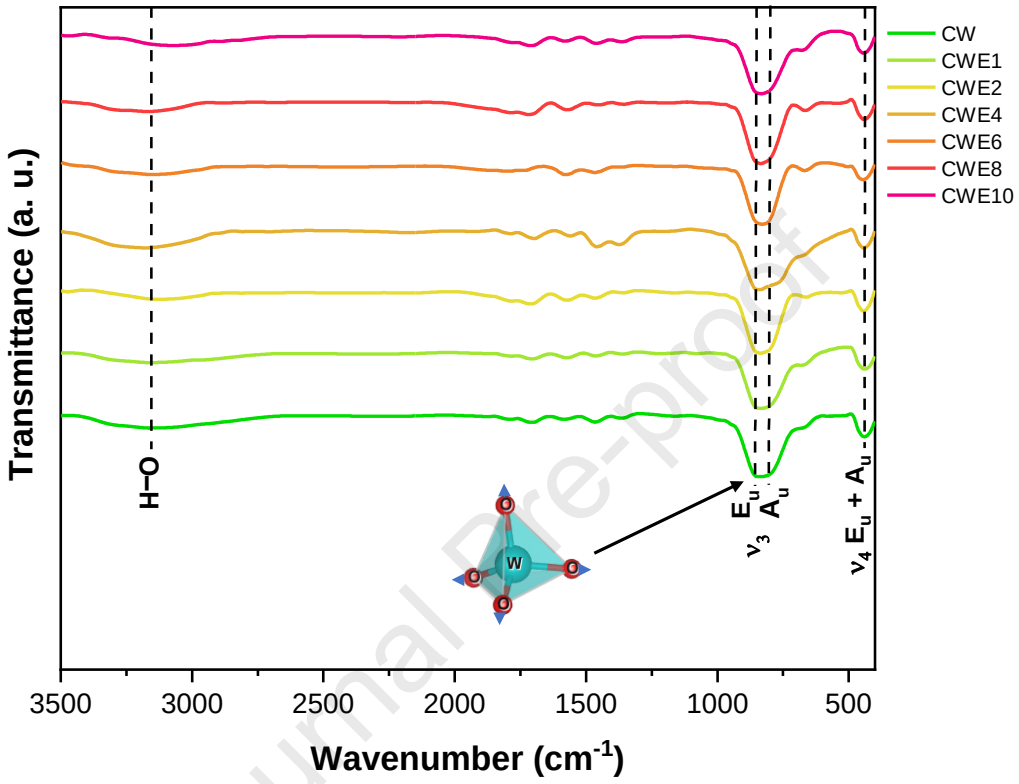

Figure SI-3. FT-IR spectra of the CW and CWE samples.

Ultraviolet-visible

The optical band gap is related to the absorbance and the photon energy by the following the equation (1).

$$h\nu\alpha \propto (h\nu - E_{gap})^{1/2} \quad (1)$$

where h is the Planck constant, ν is the frequency, α is the absorbance, and E_{gap} is the optical band gap. The CW exhibit an optical absorption spectrum governed by direct electronic

transitions characterized as n = 0.5 (n is a constant associated to the different kinds of electronic transitions).

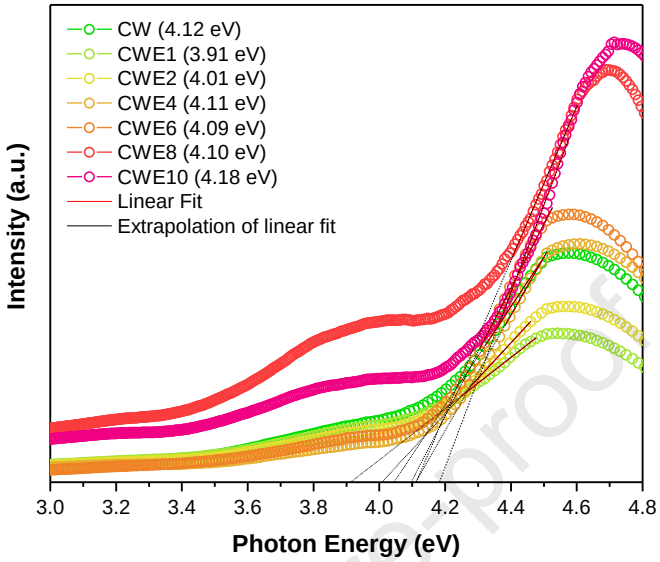

Figure SI-4. E_{gap} values obtained from the Kubelka-Munk method for CW and CWE samples.

Lifetimes

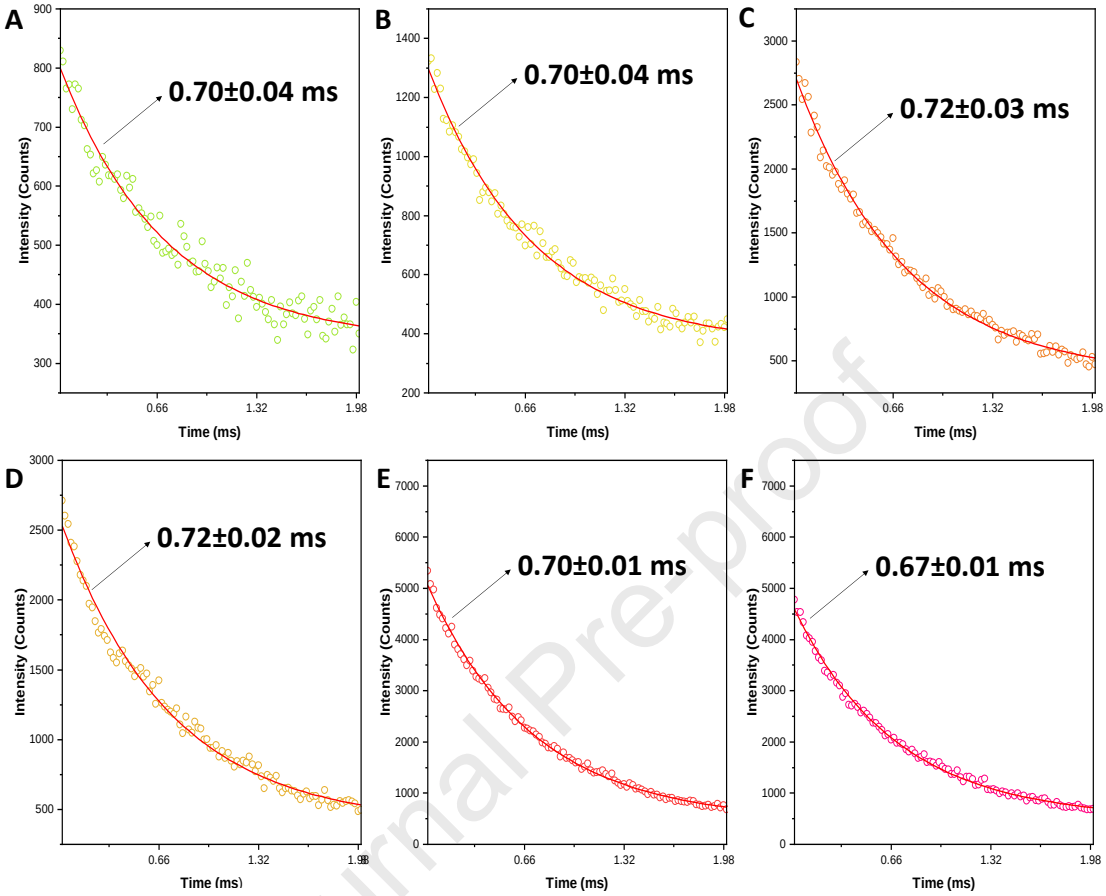

Figure SI-5. Lifetime decay curves of the $^5D_0 \rightarrow {}^7F_2$ transition for Eu^{3+} ion for **(a)** CWE1, **(b)** CWE2, **(c)** CWE4, **(d)** CWE6, **(e)** CWE8 and **(f)** CWE10.

References

1. Kumar D, Singh BP, Srivastava M, Srivastava A, Singh P, Srivastava A, et al. Structural and photoluminescence properties of thermally stable Eu^{3+} activated $CaWO_4$ nanophosphor via Li+ incorporation. J Lumin. 2018; 203:507.
2. Yu MQ, Xu HY, Li YZ, Dai QL, Wang GF, and Qin WP. Morphology luminescence and photovoltaic performance of lanthanide doped $CaWO_4$ nanocrystals. J Colloid Interface Sci. 2020; 559:162.
3. Chen LP, Gao YH, Yuan JX, Zhang QH, Yin YH, and Wang CX, *Fabrication of $CaWO_4:Eu^{3+}$ Thin Films Via Electrochemical Methods Assisted by a Novel Post Treatment*, in *Advanced Engineering Materials, Pts 1-3*, J.M. Zeng, T.S. Li, S.J. Ma, Z.Y. Jiang, and D.G. Yang, Editors. 2011. p. 2458.
4. Chen Y, Lee JH, Park SW, Moon BK, Choi BC, Jeong JH, et al., *A Novel Synthesis of $CaWO_4:Eu^{3+}$ Flower Like Microcrystals in Ethanol/water Mixed System and Characterization*, in *Materials Science and Nanotechnology I*, C.L. Zhang and L.C. Zhang, Editors. 2013. p. 512.
5. Chen DK, He DD, Lu JC, Zhong LP, Liu F, Liu JP, et al. Investigation of the role of surface lattice oxygen and bulk lattice oxygen migration of cerium-based oxygen carriers: XPS and designed H-2-TPR characterization. Appl Catal B:Environ. 2017; 218:249.
6. Ahmad MI and Bhattacharya ss. Size effect on the lattice parameters of nanocrystalline anatase. Appl Phys Lett. 2009; 95:
7. Wu HJ, Wang LD, Guo SL, Wang YM, and Shen ZY. Electromagnetic and microwave-absorbing properties of highly ordered mesoporous carbon supported by gold nanoparticles. Mater. Chem. Phys. 2012; 133:965.
8. Shpak AP, Korduban AM, Medvedskij MM, and Kandyba VO. XPS studies of active elements surface of gas sensors based on WO_{3-x} nanoparticles. J Electron Spectros Relat Phenomena. 2007; 156:172.
9. Palmqvist AEC, Wirde M, Gelius U, and Muhammed M. Surfaces of doped nanophase cerium oxide catalysts. Nanostruct Mater. 1999; 11:995.
10. Kumar S, Prakash R, Choudhary RJ, and Phase DM. Resonant photoemission spectroscopic studies of Eu2O3 thin film. J Appl Phys. 2016; 120:
11. Janbua J, Mayamae J, Wirunchit S, Baitahe R, and Vittayakorn N. Directed synthesis, growth process and optical properties of monodispersed $CaWO_4$ microspheres via a sonochemical route. RSC Adv. 2015; 5:19893.
12. Goncalves RF, Godinho MJ, Marques APA, Santos MRC, Rosa ILV, Longo E, et al. Structure, Morphology, and Optical Properties of $(Ca_{(1-3x)}Eu_{(2x)})WO_4$ Microcrystals. Electron Mater Lett. 2015; 11:193.
13. Cavalcante LS, Longo VM, Sczancoski JC, Almeida MAP, Batista AA, Varela JA, et al. Electronic structure, growth mechanism and photoluminescence of $CaWO_4$ crystals. CrystEngComm. 2012; 14:853.
14. Cavalcante LS, Sczancoski JC, Espinosa JWM, Varela JA, Pizani PS, and Longo E. Photoluminescent behavior of BaWO4 powders processed in microwave-hydrothermal. J Alloys Compd. 2009; 474:195.
15. Singh MBP and Singh RA. Color tuning in thermally stable Sm^{3+}-activated $CaWO_4$ nanophosphors. New J Chem. 2015; 39:4494.

16. Porto SPS and Scott JF. Raman Spectra of $CaWO_4$ $SrWO_4$ $CaMoO_4$ and $SrMoO_4$. Phys. Rev. 1967; 157:716.